Solvent-less method for efficient photocatalytic α-Fe2 O 3 nanoparticles using macromolecular polymeric precursors

Article *in* New Journal of Chemistry · January 2016

DOI: 10.1039/C6NJ00561F

8 authors, including:

Lorena Barrientos
Pontifical Catholic University of Chile
17 PUBLICATIONS **85** CITATIONS
SEE PROFILE

María Luisa Valenzuela Valdés
Universidad Autónoma De Chile
61 PUBLICATIONS **452** CITATIONS
SEE PROFILE

Hugh Geaney
University of Limerick
50 PUBLICATIONS **749** CITATIONS
SEE PROFILE

Colm O'Dwyer
University College Cork
189 PUBLICATIONS **1,873** CITATIONS
SEE PROFILE

NJC

PAPER

View Article Online
View Journal

Cite this: DOI: 10.1039/c6nj00561f

Solvent-less method for efficient photocatalytic α-Fe_2O_3 nanoparticles using macromolecular polymeric precursors†

Carlos Diaz,*[a] Lorena Barrientos,[bc] Daniel Carrillo,[a] Javier Valdebenito,[a] Maria L. Valenzuela,[d] Patricio Allende,[ac] Hugh Geaney[e] and Colm O'Dwyer*[ef]

Received (in Nottingham, UK)
19th February 2016,
Accepted 1st June 2016

DOI: 10.1039/c6nj00561f

www.rsc.org/njc

We report a method for solvent-less growth of single crystalline hematite Fe_2O_3 nanoparticles from metal-containing polymeric macromolecular complexes, and demonstrate their efficient photocatalytic degradation of persistent cationic dye pollutants under visible light. Macromolecular complexes such as chitosan·$(FeCl_2)_y$, chitosan·$(FeCl_3)_y$, PS-*co*-4-PVP·$(FeCl_2)_y$ and PS-*co*-4-PVP·$(FeCl_3)_y$ with controlled polymer : metal molar ratios of 1 : 1 and 5 : 1 were prepared by single reaction of the respective polymers and iron chloride salts in CH_2Cl_2. The stable insoluble compounds were characterized by elemental analysis, infra-red spectroscopy, EPR and diffuse reflectance spectroscopy, and confirm Fe salts with degrees of coordination of ~60–70%. Pyrolysis of these macromolecular precursors under air and at 800 °C forms networked Fe_2O_3 nanoparticles, whose volumetric density, size and shape is controlled by the metal content and the nature of the macromolecular complex (chitosan or PS-*co*-4-PVP). For both polymers, the 1 : 1 molar ratio precursor produces nanoparticles ranging from 10–200 nm with a moderate superparamagnetic behavior and optical bandgap marginally larger than bulk Fe_2O_3. A matrix-incubated formation mechanism involving the carbonization of the organic matter, forming voids within the macromolecular complex wherein the Fe centres coalesce, oxidize and crystallize into nanoparticles is also proposed. The hematite Fe_2O_3 nanoparticle materials demonstrate very efficient photocatalytic degradation of persistent water pollutants such as the cationic dye methylene blue. The nanoparticulate material obtained from chitosan·$(FeCl_2)_y$ 1 : 1 under the simulated sunlight (full visible spectrum) irradiation provides high rate degradation of MB by 73% in 60 min and >94% after 150 min, measured at 655 nm.

Introduction

In recent years, metal oxide nanoparticles have been the subject of intense scientific research owing to their unique physical and chemical characteristics.[1–5] The shape, size, and size distribution of these nanoparticles are the controlling factors that dictate their physical and chemical properties, and the adoption of metallic and oxide nanoparticles has facilitated significant improvement in rates and sensitivity for several forms of (photo)catalytic systems. Among the oxides, the magnetic metal oxides are very useful for particular applications[6] and iron oxides[7,8] are one of the most important magnetic nanoparticles. Iron oxide nanoparticles are typically prepared by decomposition of iron-containing precursors in the presence of an appropriate stabilizer in solution phase. However, laser-assisted decomposition, electrochemical deposition, sonochemical, and thermal processes are often required.[7] Thus the practical application in solid-state devices as sensors, supported catalysts and others requires the incorporation of the as-prepared iron nanoparticles into adequate solid matrices[9] in a single step with uniform dispersion, without requiring subsequent infiltration methods, many of which require supercritical fluids and other ultra-low dielectric constant environments or negligible surface tension for nanoparticle uptake.

Solid-state methods to synthesize Fe_2O_3 nanoparticles directly within a host material are scarcely reported, and precursor

[a] Departamento de Química, Facultad de Ciencias, Universidad de Chile, La Palmeras 3425, Nuñoa, casilla 653, Santiago de Chile, Chile. E-mail: cdiaz@uchile.cl
[b] Facultad de Química, Centro de Investigación en Nanotecnología y Materiales Avanzados CIEN-UC, Pontificia Universidad Católica de Chile, Vicuña Mackenna 4860, Macul, Santiago de Chile, Chile
[c] Center for the Development of Nanoscience and Nanotechnology, CEDENNA, Santiago, Chile
[d] Universidad Autonoma de Chile, Institute of Applied Chemical Sciences, Inorganic Chemistry and Molecular Materials Group, El Llano Subercaseaux 2801, 5° piso, San Miguel, Santiago, Chile
[e] Department of Chemistry, University College Cork, Cork, T12 YN60, Ireland. E-mail: c.odwyer@ucc.ie
[f] Micro-Nano Systems Centre, Tyndall National Institute, Lee Maltings, Cork, T12 R5CP, Ireland

† Electronic supplementary information (ESI) available. See DOI: 10.1039/c6nj00561f

(re)design is necessary to effectively control size and shape in solid-state syntheses. Bhattacharjee[10] prepared hematite Fe_2O_3 nanoparticles by thermal decomposition of ferrocene in the presence of oxalic acid at 453 K. Adhikary *et al.* prepared maghemite Fe_2O_3 nanoparticles by thermolysis of the precursor $[Fe_3O(C_6H_5COO)_6(H_2O)_3]NO_3$ at 670 °C.[11]

One approach is to reconsider the nature of the inorganic precursor itself. Chitosan[12–14] is a polysaccharide obtained by deacetylation of natural chitin, which is one of the important natural polymers constituting the shells of crustaceans and fungal cell walls. Due to NH_2 and OH groups present in the polysaccharide chains, chitosan can bind metal ions in solution forming macromolecular metal complexes.[15–17] While the ability to retain metal ions in solutions of chitosan has been widely studied, previously reported solid-state-macromolecular complexes have been not well characterized. Some Cu/chitosan complexes have been characterized by X-ray diffraction and electron spin resonance (ESR).[18,19] Chitosan can also be adapted to become a solution template/stabilizer in the formation of nanoparticles[20–28] and initial developments have shown promise for some biological applications[29,30] including biosensors for glucose detection[31] and chitosan-based nanoparticle systems have been adopted as supports for catalysts.[32] Comparatively, poly(styrene-*co*-4-vinylpyridine) is also a useful functional copolymer due to the vinylpyridine block that binds metal ions and the styrene groups that facilitate stable macromolecular complexes.[33–36] It has also been used as a ligand to aid in selective facet growth in noble metal nanoparticles.[37,38] PS-*co*-4-PVP has also been used in solution as a template/stabilizer of metals and other nanoparticles.[39–41] α-Fe_2O_3 has a band gap of 2.1 eV and while retaining its magnetic character, it is also a promising photo-induced water-splitting candidate[42,43] and amenable for other catalytic applications.[7]

To date, organic pollutants in wastewater remain one of the biggest environmental problems, because they are highly toxic and difficult to degrade.[44] A common organic contaminant is methylene blue (MB), which can be mineralized in aqueous media using Fe_2O_3 nanostructures, because they are stable and magnetically recoverable.[45] Therefore, α-Fe_2O_3 nanostructures with shape dependent catalytic properties are becoming important as recoverable additives for persistent pollutant remediation.[46] In this regard, Hou and co-workers[47] have obtained oblique and truncated nanocubes to improve visible-light photocatalytic activity; they found that the distinct photocatalytic behavior can be attributed to the diverse morphologies that are caused by different exposed crystal facets. The shape of α-Fe_2O_3 nanostructures and thus the surface free energy of the exposed crystalline facets, plays a significant role in influencing their photocatalytic properties. In this respect, Kim *et al.* have recently reported[48] a new green chemical approach to synthesize different shapes of hematite nanocrystals with exposed single crystal facets. They found a correlation between the shape, morphology and crystal facets showing a better photocatalytic performance (~90%) at 180 min of irradiation time by {104}, {100} and {001} facets of bitruncated-dodecahedron nanocrystals.

The application of nanostructured materials to electronic solid-sate devices or in high temperature technologies requires adequate solid-state methods for obtaining nanostructured materials directly in the material of interest, especially where device-sensitivity to solutions or liquids is important. Most recently, α and β phases of nanostructured Fe_2O_3 have been found as adequate host for Na and Li-ion batteries[49–51] and thus their preparation in the solid state directly on substrates[52] is an important scalable approach to phase and structure-tunable iron oxide and morphologies for Na-ion battery cathode development.

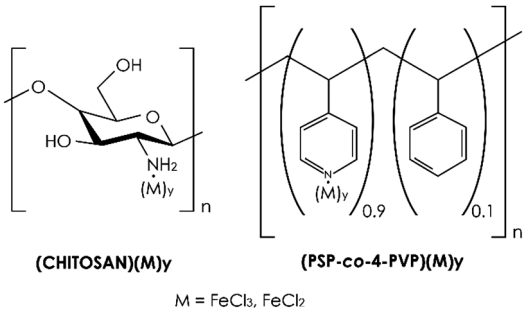

Scheme 1 Schematic representation of chitosan and PS-*co*-4-PVP and their possible coordination with metallic ions.

Here, we present a solid-state method to prepare Fe_2O_3 hematite phases by the pyrolysis of the macromolecular precursors PS-*co*-4-PVP·$(FeCl_2)_y$ (I), PS-*co*-4-PVP·$(FeCl_3)_y$ (II), chitosan·$(FeCl_2)_y$ (III) and chitosan·$(FeCl_3)_y$ (IV) (see Scheme 1) in molar ratios 1 : 1 and 5 : 1, under air and at 800 °C. Through detailed electron microscopy and diffraction measurements, in conjunction with optical reflectance spectroscopies, we detail the nature of hematite nanostructure formation in the solid state, directly on surfaces. Additionally, we present an evaluation of the photocatalytic behavior of these hematite nanostructures in the degradation of methylene blue organic pollutant in aqueous solution.

Results and discussion

Fe co-ordinated macromolecular precursors

The precursors PS-*co*-4-PVP·$(FeCl_2)_y$ (I), PS-*co*-4-PVP·$(FeCl_3)_y$ (II), chitosan·$(FeCl_2)_y$ (III) and chitosan·$(FeCl_3)_y$ (IV) in different molar ratios of 1 : 1 and 5 : 1 were prepared by direct reaction of the corresponding $FeCl_2$ and $FeCl_3$ salts and the chitosan and PS-*co*-4-PVP polymers in CH_2Cl_2 (see Methods). The contrast in molar ratio was chosen to ensure significantly different nanoparticle loading of the final composite. Owing to the insolubility of the metallic salt and the partially soluble polymer, the reaction occurs as a two-phase system. The as-obtained products are stable solids with specific color arising from the presence of the $FeCl_2$ and $FeCl_3$ salts, see Fig. S1(a) and (b) of the ESI.† The binding of the Fe salts in the polymeric chain was evidenced by UV-vis diffuse reflectance measurement of the substrate-immobilized solids, shown in Fig. 1. The broad absorption maxima were found between 450–500 nm, typical of the absorption associated with the $FeCl_2$ and $FeCl_3$ chromophore[11,53] in pre-pyrolyzed co-ordinated macromolecular complexes (see Fig. 1(a) and (c)). After pyrolytic conversion to Fe_2O_3 nanoparticles within carbonaceous matrices, Fig. 1(b) and (d) confirm predominantly

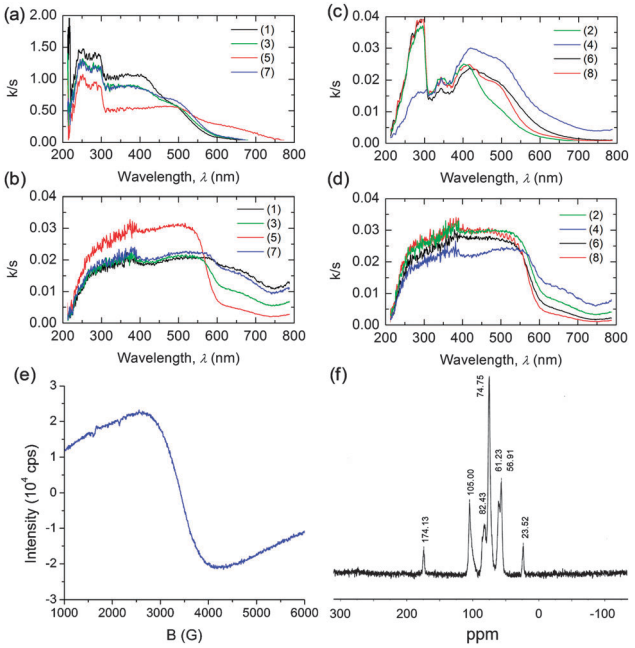

Fig. 1 UV-visible Kubelka–Munk diffuse reflectance spectra of macromolecular complexes 1, 3, 5, 7 (a) before and (b) after pyrolysis. (c) UV-visible spectra from macromolecular complexes 2, 4, 6, 8 (c) before and (d) after pyrolytic treatment. Spectra were acquired from samples in powder form after pyrolysis. (e) EPR spectra of macromolecular complex **1** and (f) ^{13}C MAS NMR spectrum of chitosan·$(FeCl_2)_y$. Reference diffuse reflectance spectra from the chitosan and PS-*co*-4-PVP are shown in Fig. S2, ESI†.

Fe_2O_3 evidenced by the defined absorption edges at ~600 nm (2.0–2.1 eV) for all precursors prepared.

The paramagnetic nature of the insoluble solids PS-*co*-4-PVP·$(FeCl_3)_y$ (II) and chitosan·$(FeCl_3)_y$ (IV) was corroborated by their EPR spectra,[54] shown in Fig. 1(e). The diamagnetic nature of the PS-*co*-4-PVP·$(FeCl_2)_y$ and chitosan·$(FeCl_2)_y$ (III) precursors was evidenced by a predominantly EPR silent response. This suggests an O_h octahedral coordination of the Fe^{2+} centers to the polymeric chain.[55] The presence of chitosan in chitosan·$(FeCl_2)_y$ precursors was corroborated by ^{13}C MAS NMR spectroscopy. As shown in Fig. 1(f), the typical bands of chitosan[55,56] were observed. The C_1 signal at 105 ppm is assigned to the C_1 carbon of the O–C_1H(O)–C moiety. Numeration of the carbon in the cycle followed that of ref. 55. Similarly, the other signals were assigned to C_2 at 56.91 ppm from the C–C_2H(NH_2)C moiety, C_3–C_5 at 74.75 ppm from (C_3) C–C_3H(OH)–C, (C_4) C–C_4H(OH)–C at 82.43 ppm, and (C_5) C–C_5(O)C and (C_6) C–C_6H_2(OH) at 61.23 ppm. Additionally, as is commonly observed in chitosan, signals in NMR spectra characteristic of a degree of acetylation are observed at 174.13 ppm (C═O) and at 23.52 ppm (CH_3). As observed for other metal–polymer complexes,[56] the chitosan was not adversely modified after coordination according to the ^{13}C MAS NMR spectra and remained an effective co-ordination host to metal centers.

The degree of coordination of the Fe centers into the polymeric chain was estimated from elemental analysis and by TG/DSC analysis. Coordination values between 60–70% were found. Additionally, the coordination was confirmed by the IR spectral bands for the chitosan as well as the poly(styrene-*co*-4-vinylpyridine) polymers. The broad ν(OH) + ν(NH) observed at 3448 cm^{-1} of free chitosan becomes unfolded upon coordination, shifting to the range 3345–3398 cm^{-1} for the macromolecular complexes (III) and (IV).[57–60] For the PS-*co*-4-PVP polymer-based complexes (I) and (II), the pyridine coordination is shown *via* the emergence of a new band centered at 1600 cm^{-1} (ref. 61) (see ESI†).

Pyrolytic production of hematite Fe_2O_3 nanoparticles

The X-ray diffraction (XRD) pattern (see Fig. S3, ESI†) confirms that the as-prepared powders are hematite (α-Fe_2O_3) structures with a high degree of crystallinity in multigram scale quantity from the solid-state synthetic route.[62,63] SEM analysis in Fig. 2a from the pyrolyzed chitosan·$(FeCl_3)_y$ (in ratio 1 : 1) precursor shows a morphology or irregular fused grains with varied size typical of nanostructured oxides obtained from a solid-state method.[9] EDS analysis in Fig. 2c confirms the presence of iron and oxygen atoms in a stoichiometric ratio for this phase.

Fig. 2b shows a typical SEM image of the as-prepared product from pyrolysis of the chitosan·$(FeCl_3)_y$ precursor in a 5 : 1 ratio. Morphological examination by SEM evidenced irregularly shaped particles comprising the powder with some compacted zones and other 3-D mesh-like porous regions also typical of nanostructured oxides obtained from a pyrolytic solid-state methods. Importantly, the morphology is independent of the stoichiometrically consistent phase for this product, which remains consistent throughout the powder.

The low-magnification TEM images for pyrolytic product from the 1 : 1 chitosan·$(FeCl_3)_y$ precursor (Fig. 3(a)) show agglomerates composed of fused assemblies of individual nanoparticles. HRTEM analysis in Fig. 3(c) and associated electron diffraction pattern (Fig. 3(d)), exhibit characteristic atomic lattice spacings in the nanoparticle structure corresponding to the (110) planes

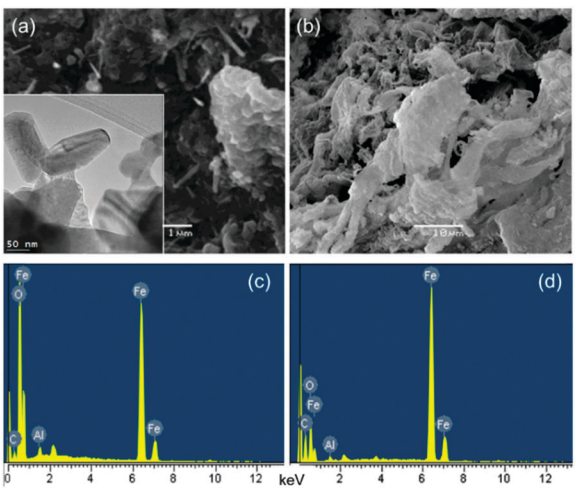

Fig. 2 (a) SEM image of the product from pyrolysis of the chitosan·$(FeCl_3)_y$ precursors in 1 : 1 ratio (the inset shows a TEM image of individual nanoparticles) and (b) from the chitosan·$(FeCl_3)_n$ precursor in a 1 : 5 ratio. (c and d) The EDX spectra confirm Fe and O presence and successful elimination of Cl from both precursors during hematite formation. The Al signal is from the sample stub.

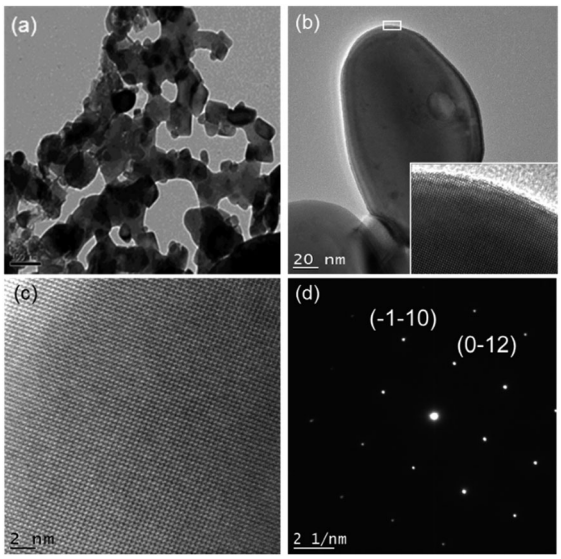

Fig. 3 (a) TEM image of the fused nanoparticulate structure of the pyrolyzed hematite from the 1 : 1 chitosan·$(FeCl_3)_y$ precursor. HRTEM examination in (b) and (c) confirms single crystal structure indexed to trigonal hematite (space group $R\bar{3}c$) in the electron diffraction pattern in (d).

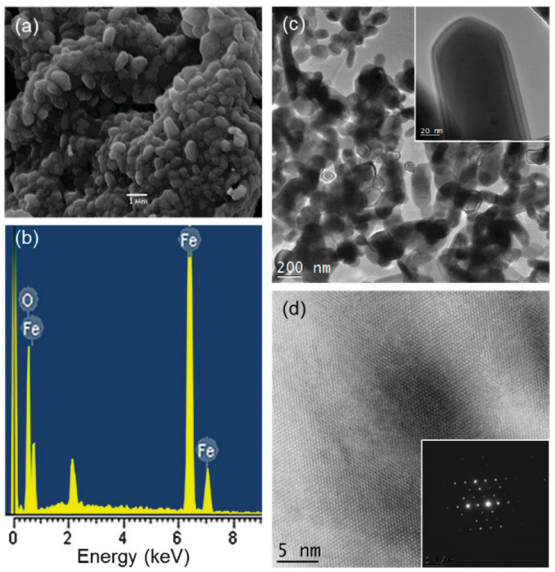

Fig. 5 (a) SEM, (b) EDS, (c) TEM, and (d) HRTEM analysis of the pyrolytic crystalline materials from 1 : 1 chitosan·$(FeCl_2)_y$ precursors. Contrast in (d) arises from thickness variations.

of hematite α-Fe_2O_3 consistent with space group $R\bar{3}c$ with a = 5.0356 Å, c = 13.7489 Å. In all precursors, complete pyrolysis consistently results in α-Fe_2O_3 and no intermediate akaganeite (β-FeOOH) phases are observed.

SEM images for the pyrolytic product from the precursor PS-*co*-4-PVP·$(FeCl_3)_y$ ratio 1 : 1 exhibited a mixture of morphologies, see Fig. S4, ESI†. Figure shows how the resulting haemetite develops a raceme-like morphology, comprising nanoscale branched features on bulk crystalline backbones. TEM analysis in Fig. 4(a) and (b) confirms the formation of nanoparticles of α-Fe_2O_3 crystals in fused agglomerates, with a consistent average size of 150–200 nm. The resulting nanoparticle are also single crystalline Fe_2O_3, as shown in HRTEM image in Fig. 4(c). A similar morphology has been observed for another nanostructured iron oxides obtained from solution methods,[8,62,63] suggesting a similar crystallization mechanism of oxidized Fe species but in the solid state, as will be detailed further on.

A specifically different morphology to that obtained for pyrolytic precursors from precursor PS-*co*-4-PVP·$(FeCl_3)_y$ 1 : 1 was obtained from PS-*co*-4-PVP·$(FeCl_3)_y$ 5 : 1 where formless structures typical of powdered products were observed, see S5, ESI†.

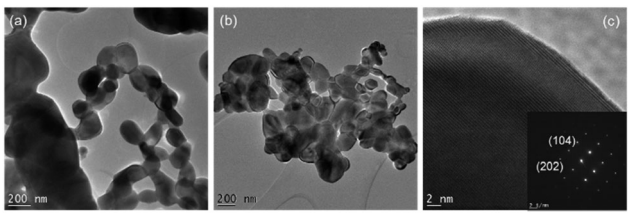

Fig. 4 (a and b) TEM images of the pyrolytic fused nanocrystal product from the PS-*co*-4-PVP·$(FeCl_3)_y$ precursor (c) HRTEM image of the single crystalline structure of Fe_2O_3 nanoparticles.

TEM analysis in Fig. 5 demonstrates that the microstructure of the powder particles comprised networks of fused nanoparticles with single crystal hematite crystal structure. This is typical of the pyrolyzed structures that are formed (*vide infra*) when a limited and sparse density of nanoparticles from low Fe content in the precursor (compared to the polymer volume fraction) are rapidly formed in the earlier stages (lower temperatures) of pyrolysis. In such cases, the higher pyrolysis steps decompose the surrounding matrix materials that incubate the already formed nanoparticle in the voids created by outgassing. Subsequent full pyrolytic decomposition of the carbonaceous matrix allows non-oriented attachment and nanoparticle fusing (but not Ostwald or similar ripening) to occur to form a high surface area random network of quasi-linear nanoparticulate chains that are folded into larger porous powder particles. A similar situation is found for the chitosan·$(FeCl_2)_y$ precursor with a similar 5 : 1 ratio (see S6, ESI†).

Optical properties of substrate-immobilized solid state Fe_2O_3 nanopowders

Hematite is an n-type semiconductor (E_g = 2.1 eV at RT assuming bulk electron and hole effective masses). For the nanostructured α-Fe_2O_3 this band-gap value can be increased by quantum confinement, extending the absorption edge from 2.1 to >4.0 eV.[64,65] However, for micrometric structures comprising larger nanocrystals in the form of agglomerates, the absorption edge is located close to 2.1 eV (products from precursors (1) and (4)), as demonstrated from optical absorbance data of large deposits of the product in Fig. 6. The products from these precursors typically have a higher metal content and thus a higher density of larger oxide particles. For the as-prepared powders with lower metal : polymer ratios, the effective optical transitions determined from visible absorbance measurements

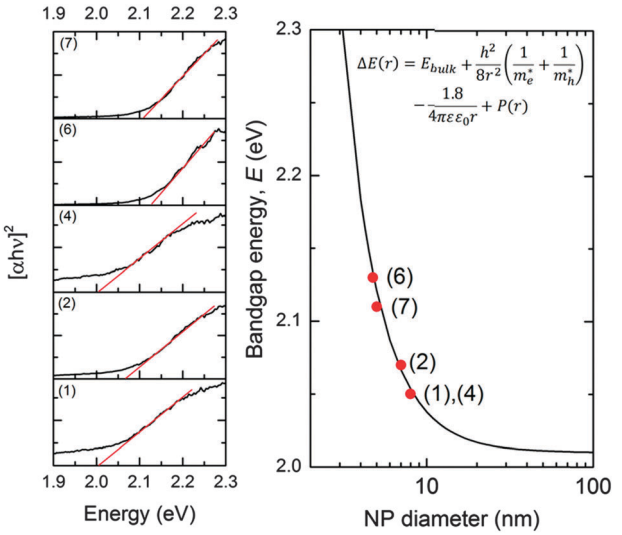

Fig. 6 Tauc plots derived from UV-vis transmission spectra for the Fe_2O_3 prepared from macromolecular precursors. The extrapolated band gap energies are also plotted against the theoretical prediction for direct allowed optical transitions of the band gap with quantum confinement effects as a function of nanoparticle radius. Here, $\Delta E(r)$ is the band-gap of the nanoparticles, E_{bulk} is the band-gap of bulk Fe_2O_3, m_e* and m_h* are the effective masses of electrons and holes in Fe_2O_3 (fitted effective masses of $m_e^* = m_h^* = 0.27m_0$ were used, where $m_0 = 9.11 \times 10^{-31}$ kg is the free-electron mass).

in the framework of the Tauc model for direct allowed optical transitions consistent with quantum confinement.

As shown in Fig. 6, and the absorption edge extrapolation confirms band gap energies higher than bulk values[43,65] and the fitting to an infinite square potential well contribution with $1/R^2$ dependence shows that the optical band gap from these powdered materials arises from sub-10 nm nanoparticles contained within voids of pyrolyzed carbonaceous products with lower metal content, and thus spatially distributed, smaller Fe_2O_3. We believe that the fused agglomerates must also contain smaller nanoparticulate oxide that contributes to confined emission energies since the diffuse scattering by the carbon matrix does not contribute to increase effective absorption edges. The coulombic interaction of excitons and spatial correlation corrections ($P(r)$) were included but negligibly affected the band gap energy values due to the high dielectric constant (>81) of Fe_2O_3.

Iron oxides are very important technologically because of their magnetic properties.[7,8] The magnetic characterization measurements of Fe_2O_3 obtained from the pyrolytic products from the precursors chitosan·$(FeCl_3)_y$ and PS-*co*-4-PVP·$(FeCl_3)_y$ shown in Fig. S7, ESI,† suggest that the α-Fe_2O_3 nanoparticles exhibit superparamagnetic behavior. This has been observed for nanoparticles <10 nm in size, and the measurements further confirm a smaller length scale Fe_2O_3 nanoparticle contribution in addition to the primary 100–200 nm nanoparticle agglomerates formed in the solid state. However, some reports have claimed similar behavior for iron oxide/silica nanocomposites.[66] Agglomerates of hematites particle have also been reported to exhibit coercivity two times greater than that of commercial hematite.[67] From Fig. S7 (ESI†), we determined that the saturated magnetization is enhanced for the pyrolytic products from the chitosan·$(FeCl_3)_y$ compared to the PS-*co*-4-PVP·$(FeCl_3)_y$ macromolecular precursors. The magnetic behavior from preliminary magnetization measurements is similar to those observed for hematite nanoparticles obtained by aqueous precipitation methods,[68] consistent with nanoparticles <20 nm, features sizes smaller than the fused crystallites.

Formation mechanism of matrix-loaded Fe_2O_3 nanoparticles. Although the formation of single phase crystalline nanoparticles in solution is well-known[69] under a variety of conditions, the formation mechanism in solid-state is lacking[70,71] and its development is important for materials that are sensitive to liquid/solvent environments, or that require a demixing-mediated crystallization process that infers thorough porosity throughout the powder.

The formation mechanism of the solid-state Fe_2O_3 nanostructures in this work can be compared to other investigations.[70] The first step on heating involves the formation of a 3D network to produce a thermally[72] stable matrix or host, shown in Fig. 7A. This shows details of the first heating step, a process whereby crosslinking of the polymer by Fe^{3+} ions causing a chain scission process.

This first step is crucial to offset sublimation. For instance, ferrocene undergoes sublimation on heating at 483 K (the melting point), but in presence of oxalic acid, nanoparticles of Fe_2O_3 nanoparticles are formed.[10] In our system, which does not use ferrocene, the first heating step likely involves a cross-linking of

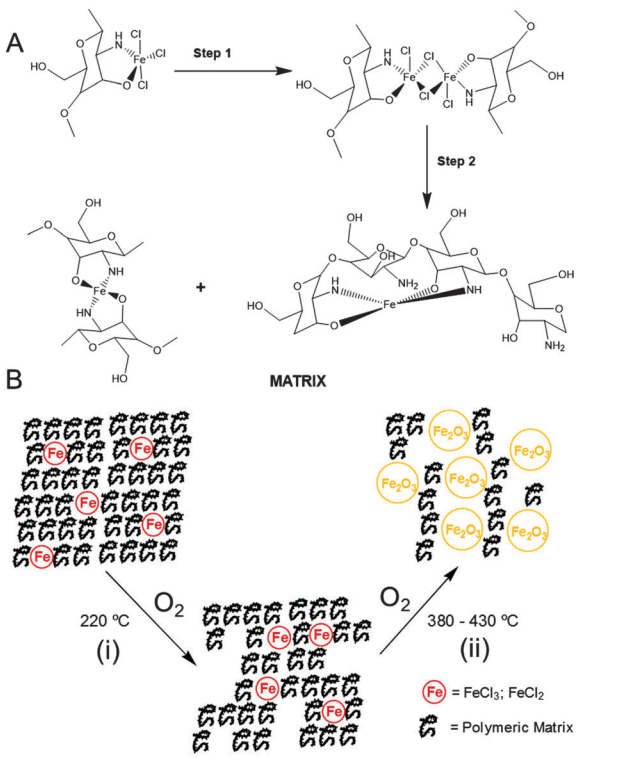

Fig. 7 Schematic representation of the possible mechanism in the formation of Fe_2O_3 nanoparticles from the decomposition of the various precursors. (A) Coordination model of $FeCl_2$ to chitosan. (B) Representation of pyrolytic decomposition including chain scission, oxidation and crystallization of Fe_2O_3 from the macromolecular complexes.

the chitosan (5–8) and PS-*co*-4-PVP (1–4) polymer precursors to create a 3D matrix containing O–Fe–O and H_2N–Fe–NH_2 linkages (for the chitosan polymer) and (pyridine)N–Fe–N(pyridine) bonds for the PS-*co*-4-PVP polymer (see Fig. 7A). The successive steps involve the initiation of the organic carbonization, with holes or voids produced where the nanoparticles are able to nucleate. According to TG/DSC analysis, this occurs at ~400 °C for the chitosan and 360 °C for PS-*co*-4-PVP polymer matrices. Simultaneously, the oxygen of the air oxidizes the Fe(II) from the $FeCl_2$ salt to Fe(III) with the formation of Fe_2O_3, which nucleates in nanoparticulate form inside the holes formed by the combustion of the organic matter (schematically represented in Fig. 7B). In the intermediate stage a layered graphitic carbon host was detected[70] that acts as template were the nanoparticles can coalesce and crystallize into their respective morphologies. After complete combustion, this template is fully decomposed, forming a residual carbon that houses the smallest <20 nm nanoparticles.[9] Materials that comprise larger powder particles that are themselves arrangements of nanoparticles with fused morphologies, are typical products formed from precursors with higher metal content. Higher polymer fraction precursors provide more carbon to create the host, and a lower metal content to nucleate and grow nanoparticles <20 nm.

Photocatalytic behavior of Fe_2O_3 nanoparticles. The photocatalytic behavior of α-Fe_2O_3 nanostructure-containing powders were investigated by quantifying the degradation of MB under UV (330–400 nm) and also by visible light (400–670 nm), and the absorbance spectra over the entire MB degradation are shown in Fig. 8(a) and (b). The typical degradation curves of MB with α-Fe_2O_3 from chitosan·$(FeCl_2)$ 1 : 1 and α-Fe_2O_3 from PS-*co*-4-PVP·$(FeCl_2)$ 1 : 1 are shown in Fig. 8c. The photocatalytic reaction of semiconductor materials follows $-\ln(C/C_0) = kt$, where the k is the apparent pseudo-first-order rate constant for this degradation process, for a constant α-Fe_2O_3 concentration (determined as shown in Fig. S8, ESI†). In Fig. 8c, the k value and thus degradation rate are determined with the photocatalytic performance at 60 min and 150 min of irradiation time summarized in Table 1. In absence of the photocatalyst, we observed slight degradation of MB (~6.6%), indicating a limited self-photodegradation of MB molecules under UV-Vis irradiation (see Fig. 8c). A highest extent of MB degradation (98.6%) at 150 min of irradiation time was achieved for α-Fe_2O_3 from PS-*co*-4-PVP·$(FeCl_2)_y$ product formed from the precursor with a 1 : 1 ratio.

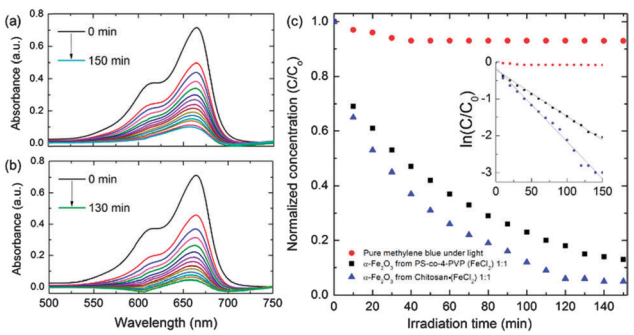

Fig. 8 (a) Degradation curves of MB in presence of (a) α-Fe_2O_3·PS-*co*-4-PVP, (b) α-Fe_2O_3·chitosan. (c) Normalized concentration changing of MB without catalyst, in presence of α-Fe_2O_3·PS-*co*-4-PVP and in presence of α-Fe_2O_3·chitosan.

Table 1 Kinetic data for the degradation of MB with α-Fe_2O_3 obtained from PS-*co*-4-PVP and chitosan macromolecular precursor

Photocatalyst	Apparent photodegradation rate constant k (10^{-2} min^{-1})	Decoloration rate η (%) at 60 min	Decoloration rate η (%) at 150 min
α-Fe_2O_3 from PS-*co*-4-PVP·$(FeCl_2)_y$ 1 : 1	1.2 ± 0.04	62.6	86.9
α-Fe_2O_3 from chitosan·$(FeCl_2)_y$ 1 : 1	2.1 ± 0.1	73.4	94.6

The size and morphology of two systems were determined by electron microscopy studies earlier, showing fused nanoparticles and 3D networks with average sizes of 150–200 nm for α-Fe_2O_3 from chitosan·$(FeCl_2)$ and 1 : 1 and 55–100 nm for α-Fe_2O_3 from PS-*co*-4-PVP·$(FeCl_2)$ and 1 : 1. These morphologies show a high surface area random network of quasi-linear that nanoparticulate chains are folded into larger porous powder particles.

Optical absorption and magnetic susceptibility measurements indicate smaller nanoparticles that also contribute to efficient photocatalysis by increasing the chemical reactivity of these nanostructures of a pure hematite phase. To our knowledge, this approach provides the first evidence of all solid state production of nanoparticle of single crystalline, pure Fe_2O_3 with highly efficient photocatalytic behavior of pristine nanostructures for degradation of organic pollutants, such as MB.[73–78] Ayachi and co-workers[79] have reported hematite Fe_2O_3 nanoplatelets with a MB photocatalytic degradation of 47% after 4.5 h of irradiation time. To compare the efficiency of our system, we note that many literature reports with better photocatalytic performance using Fe_2O_3 often use host materials or hetero-nanostructures using oxide with significant UV absorption and electronic conductivities such as Fe_2O_3@TiO_2, systems with ~98–100% reported efficiency, or Fe_2O_3–TiO_2 using Al, Zn, Cu or α-Fe_2O_3/Bi_2MoO_6 (23–70%) to degrade MB, Rhodamine B, 2,4-dichlorophenoxyacetic acid, malachite green and acid orange 7 at 90–150 min.[46,80–82]

Conclusions

A facile macromolecular metal complex synthetic route has been developed for preparing hematite Fe_2O_3 nanostructured materials in the absence of solvents. The chitosan·$(FeCl_2)_y$ precursor facilitates the formation of single crystalline nanoparticles within the matrix host during pyrolysis, while coordination of Fe centres from an Fe(III) salt to PS-*co*-4-PVP also induces the formation hematite nanoparticles within a decomposable host matrix. All are formed in the absence of solvent or liquids at all stages. The metal : polymer molar ratio was found to influence the particle size, with the 1 : 1 ratio facilitating fused networks of spheroidal nanoparticles as a porous material. Magnetic susceptibility and optical absorption measurements indicated sub-20 nm nanoparticles are formed within the matrix in addition to the fused network of crystalline nanoparticle materials.

The work demonstrates the possibility to control the particle size and morphology through the nature of the Fe salt, the polymer macromolecule, and the molar ratio which together influence the volumetric density and size of the nanoparticles in the carbonaceous matrix formed by decomposition of the polymer. This method may also provide porous iron oxide electrode materials for Na-ion and Li-ion batteries that can be grown directly onto the current collector or other substrates, and for sensors, catalysts and other applications requiring nanoparticles of Fe_2O_3, but whose preparation protocols are sensitive to liquids, solvents or solution-based synthetic conditions. Depending on the macromolecular–polymer ratio and the nature of the decomposition, this synthetic approach provides a range of porous iron oxide material structures that are accessible to electrolyte or for site-selective placement and conversion *via* coating methods and thermal, ozone or other polymeric decomposition methods. The Fe_2O_3 nanoparticle materials have a high porosity and surface area and were demonstrated to be very efficient photocatalysts capable of degrading and removing recalcitrant water pollutants such as cationic dyes under full visible light irradiation. Specifically, degradation (decolouration rates) from photocatalysis achieve $>94\%$ after 150 min in the visible range (at 655 nm).

Methods

Chitosan, poly(styrene-*co*-4-vinylpyridine) and $FeCl_2{\cdot}4H_2O$ were purchased from Aldrich, $FeCl_3{\cdot}6H_2O$ was purchased from Merck. Chitosan of low molecular weight was used as received. An estimation of the molecular weight was performed by viscosimetry. The average molecular weight was determined from the Mark–Houwink–Sakurada relation and the values of $[\eta]$ were obtained using parameters previously reported by Rinaudo *et al.*[20] The determination was performed in aqueous solution in presence of NaCl, acetic acid and urea. The obtained value was M_w = 61 000 g mol^{-1}. Poly(styrene-*co*-4-vinylpyridine) with 90% of pyridine groups was used as received.

Preparation of the macromolecular precursors

In a typical preparation the $FeCl_3$ or the $FeCl_2$ salt was added in a Schlenk tube over a CH_2Cl_2 solvent (50 mL) under magnetic stirring and then each one of the respective polymers, PS-*co*-4-PVP or chitosan were added amounts according to a 1 : 1 or 1 : 5 molar ratios metal/polymer for between 7 to 10 days. Other details for each metallic salts reaction are provided in Table S1, in the ESI.† Subsequently, the supernatant solution (if the solid decanted) was extracted with a syringe and the solid was dried under vacuum. Where required, the solution was dried under vacuum and the resulting solid was further dried.

Characterization

Solid pyrolytic samples were characterized by X-ray diffraction (XRD), scanning electron microscopy (SEM), high resolution transmission electron microscopy (HR-TEM) and Fourier transform infra-red (FT-IR) spectroscopy. SEM was acquired with a JEOL JSM-6380LV. Energy dispersive X-ray analysis (EDX) was performed on a NORAN Instrument micro-probe. transmission electron microscopy (TEM) data were acquired using a JEOL JEM-1200 EX II operating at 120 kV with images taken with a ES500W Erlangshen CCD Camera, and HR-TEM with a JEOL 2100 TEM operating at 200 kV. The TEM samples were prepared by dispersing pyrolized material onto copper grids and dried at room temperature. XRD was conducted at room temperature on a Siemens D-5000 diffractometer with θ–2θ geometry. The XRD data was collected using a Cu-Kα radiation (40 kV, 30 mA). FT-IR measurements were performed on a Perkin Elmer FT-IR spectrophotometer model Spectrum BX-II. Thermogravimetric analysis (TGA) and differential scanning calorimetry (DSC) measurements were performed on a Mettler TA 4000 instrument and Mettler DSC 300 differential scanning calorimeter, respectively. The polymer samples were heated at a rate of 10 °C min^{-1} from ambient temperature to 1000 °C under a constant flow of oxygen.

Magic angle spinning (MAS) nuclear magnetic resonance (NMR) spectra were obtained using an Oxford wide bore 9.4 T magnet equipped with a Bruker Avance II console and employing a 4 mm H/X-CPMAS probe. For all samples, ^{1}H–^{13}C, cross polarization (CP) experiments were acquired using a CP mixing time of 2 ms. For ^{13}C experiments the spectral frequency was 100.577 MHz and the NMR chemical shifts were externally referenced to adamantane (major peak positioned at 38.6 ppm).

Photocatalytic organic pollutant degradation

Methylene blue (MB) was used as a model dye compound to test the photocatalytic degradation behavior of the hematite nanostructures. The photocatalytic activity was evaluated by measuring the bleaching rate of MB under UV-Vis illumination in the range 330–700 nm at room temperature using a $CuSO_4$ filter (0.1 mol L^{-1}), to avoid the self-degradation and thermal catalytic effects of this organic pollutant. A quartz tube of 20 mL was used as a photoreactor vessel. The optical system used was a xenon lamp (150 W) positioned 15 cm from the photoreactor. 15 mg of the photocatalyst and 15 mL of MB aqueous solution (1×10^{-5} mol L^{-1}) underwent continuous magnetic stirring. Prior to irradiation, the suspension was stirred in the darkness for 30 min to establish an adsorption/desorption equilibrium, after which the photocatalytic degradation of MB was initiated. Samples were withdrawn from the reactor at certain time intervals (10 min), and centrifuged to remove the particles. Photodegradation was monitored by measuring the absorbance of the solution at 655 nm.

Acknowledgements

The authors acknowledge Fondecyt Projects 1120179, 1160241 and 1131112 for financial support. L. B. acknowledges the Basal Financing Program CONICYT FB0807 (CEDENNA). The authors would like to acknowledge Dr Juliano Denardin from the Departamento de Física, Universidad de Santiago for magnetic measurements. This research has received funding from the European Commission Seventh Framework Programme FP7/2007–2013 (Project STABLE) under grant agreement no. 314508.

References

1 Y. Mai, F. Zhang and X. Feng, *Nanoscale*, 2014, **6**, 106–121.
2 J. B. Goodenough, *Chem. Mater.*, 2014, **26**, 820–829.
3 T. Nguyen, *Nanoscale*, 2013, **5**, 9455–9482.
4 J. Lee, S. Zhang and S. Sun, *Chem. Mater.*, 2013, **25**, 1293–1304.
5 P. Poizot, S. Lauruelle, S. Grugeon, L. Dupont and J. M. Tarascon, *Nature*, 2000, **407**, 496–499.
6 K. Sivula, *J. Phys. Chem. Lett.*, 2013, **4**, 1624–1633.
7 S. Laurent, D. Forge, M. Port, A. Roch, C. Robic, L. Vander Elst and R. N. Muller, *Chem. Rev.*, 2008, **108**, 2064–2110.
8 A. S. Teja and P. K. Ko, *Prog. Cryst. Growth Charact. Mater.*, 2009, **55**, 22–45.
9 C. Díaz and M. L. Valenzuela, in *Metallic Nanostructures Using Oligo and Polyphosphazenes as Template or Stabilizer in Solid State*, ed. H. S Nalwa, Encyclopedia of Nanoscience and Nanotechnology, American Scientific Publishers, California, 2010, vol. 16, pp. 239–256.
10 A. Bhattacharjee, A. Rooj, M. Roy, J. Kusz and P. Guthich, *J. Mater. Sci.*, 2013, **48**, 2961–2968.
11 A. Kumar-Dutta, S. Kumar and B. Adhikary, *Mater. Res. Bull.*, 2014, **49**, 28–34.
12 K. Desai, K. Kit, J. Jiajie and S. Zivanovic, *Biomacromolecules*, 2008, **9**, 1000–1006.
13 Q. Li, E. T. Dunn, E. W. Grandmaison and M. F. Goosen, *J. Bioact. Compat. Polym.*, 1992, **7**, 370–397.
14 I. Aranaz, M. Mengibar, R. Harris, I. Paños, B. Miralles, N. Acosta, G. Galed and A. Heras, *Curr. Chem. Biol.*, 2009, **3**, 203–230.
15 R. B. Hernandez, O. Reyes and A. L. R. Merce, *J. Braz. Chem. Soc.*, 2007, **18**, 1388–1396.
16 I. S. Lima and C. Airoldi, *Thermochim. Acta*, 2004, **421**, 133–139.
17 E. Taboada, G. Cabrera and G. Cardenas, *J. Chil. Chem. Soc.*, 2003, **48**, 7–129.
18 K. Ogawa, *Chem. Mater.*, 1993, **5**, 726–728.
19 S. Schlick, *Macromolecules*, 1986, **19**, 192–195.
20 J. Brugnerotto, J. Lizardi, F. M. Goycoolea, W. Arguelles-Monal, J. Desbrieres and M. Rinaudo, *Polymer*, 2001, **42**, 3569–3580.
21 H. Huang and X. Yang, *Carbohydr. Res.*, 2004, **339**, 2627–2631.
22 Y. Ding, X. H. Xia and X. Zhang, *Nanotechnology*, 2006, **17**, 4156–4162.
23 M. Adlim, M. A. Bakar, K. Kong Live and J. Ismail, *J. Mol. Catal. A: Chem.*, 2004, **212**, 141–149.
24 K. Okitsu, Y. Mizukoshi, T. A. Yamamoto, Y. Maeda and Y. Nagata, *Mater. Lett.*, 2007, **61**, 3429–3431.
25 K. H. Yang, Y. Ch. Liu, T. Ch. Hsu and H. I. Tsai, *Mater. Res. Bull.*, 2010, **45**, 63–68.
26 I. Zhitomirsky and A. Hashambhoy, *J. Mater. Process. Technol.*, 2007, **191**, 68–72.
27 H. Huang, Q. Yuan and X. Yang, *Colloids Surf., B*, 2004, **39**, 31–37.
28 Y. Ch. Chang and D. H. Chen, *J. Colloid Interface Sci.*, 2005, **283**, 446–451.
29 L. Ding, Ch. Hao, Y. Xue and H. A. Ju, *Biomacromolecules*, 2007, **8**, 1341–1346.
30 Y. Du, X. L. Luo, J. J. Xu and H. Y. Chen, *Bioelectrochemistry*, 2007, **70**, 342–347.
31 X. L. Luo, J. J. Xu, Q. Zhang, G. L. Yang and H. Y. Chen, *Biosens. Bioelectron.*, 2005, **21**, 190–196.
32 E. Guibal, *Prog. Polym. Sci.*, 2005, **30**, 71–109.
33 P. Guo, W. Wenyan, G. Liang and P. Yao, *J. Colloid Interface Sci.*, 2008, **323**, 229–234.
34 L. A. Belfiore, M. P. Curdie and E. Ueda, *Macromolecules*, 1993, **26**, 6908–6917.
35 A. Haynes, P. M. Maitlis, R. Quyoum, C. Pulling, H. Adams, S. E. Spey and R. W. Strange, *J. Chem. Soc., Dalton Trans.*, 2002, 2565–2572.
36 C. V. Franco, M. M. Da Silva Paula, G. Goulart, L. F. De Lima, L. K. Noda and N. S. Gonçalves, *Mater. Lett.*, 2006, **60**, 2549–2553.
37 J. Xian, Q. Hua, Z. Jiang, Y. Ma and W. Huang, *Langmuir*, 2012, **28**, 6736–6741.
38 G. Collins, M. Schmidt, G. McGlacken, C. O'Dwyer and J. D. Holmes, *J. Phys. Chem. C*, 2014, **118**, 6522–6530.
39 F. Wen, W. Zhang, G. Wei, Y. Wang, J. Zhang, M. Zhang and L. Shi, *Chem. Mater.*, 2008, **20**, 2144–2150.
40 S. Klingelfer, W. Heitz, A. Greiner, S. Oestreich, S. Forster and M. Antoinietti, *J. Am. Chem. Soc.*, 1997, **119**, 10116–10120.
41 P. Zheng, X. Jiang, X. Zhang and L. Shi, *Langmuir*, 2006, **22**, 9393–9396.
42 A. Hellman and R. S. Pala, *J. Phys. Chem. C*, 2011, **115**, 1290–12907.
43 M. F. AlKuhali, M. Saleem and S. M. Durrani, *J. Alloys Compd.*, 2012, **521**, 178–182.
44 C. C. Wang, J. R. Li, X. L. Lv, Y. Q. Zhang and G. Guo, *Energy Environ. Sci.*, 2014, **7**, 2831.
45 S. Rehman, W. Yang, F. Liu, Yu. Hong, T. Wang and Y. Hou, *Inorg. Chem. Front.*, 2015, **2**, 576–583.
46 J. Liu, S. Yang, W. Wu, Q. Tian, S. Cui, Z. Dai, F. Ren, X. Xiao and C. Jiang, *ACS Sustainable Chem. Eng.*, 2015, **3**, 2975–2984.
47 W. Wu, R. Hao, F. Liu, X. Su and Y. Hou, *J. Mater. Chem. A*, 2013, **1**, 6888–6894.
48 A. K. Patra, S. K. Kundu, A. Bhaumikb and D. Kim, *Nanoscale*, 2016, **8**, 36–377.
49 B. Koo, H. Xiong, M. Slater, V. Prakapenka, M. Balasubramanian, P. Podsiadlo, C. Johnson, T. Rajh and E. Shevchenko, *Nano Lett.*, 2012, **12**, 2429–2435.
50 B. Koo, S. Chattopadhyay, T. Shibata, V. Prakapenka, C. Johnson, T. Rajh and E. Shevchenko, *Chem. Mater.*, 2013, **25**, 245–252.
51 M. Valvo, F. Lindgren, U. Lafont, F. Bjorefors and K. Edstrom, *J. Power Sources*, 2014, **245**, 967–978.
52 C. Díaz, M. L. Valenzuela, V. Lavayen, K. Mendoza, D. O. Peña and C. O'Dwyer, *Inorg. Chim. Acta*, 2011, **377**, 5–13.
53 N. Cuello, V. Elias, S. Urreta, M. Oliva and G. Eimer, *Mater. Res. Bull.*, 2013, **48**, 3559–3563.
54 N. M. Figgis, *Introduction to Ligand Fields*, John Wiley and Sons, New York, 1966.
55 H. Saito, R. Tabeta and K. Ogawa, *Macromolecules*, 1987, **20**, 2424–2430.
56 L. Heux, J. Brugnerotto, J. Desbrieres, M. F. Versali and M. Rinaudo, *Biomacromolecules*, 2000, **1**, 746–751.

57 S. Adewuyi, K. T. Karem, A. O. Atayese, C. A. Amolegbe and C. A. Akinremi, *Int. J. Biol. Macromol.*, 2011, **48**, 301–303.
58 E. J. Baran, *Carbohydr. Polym.*, 2008, **74**, 704–706.
59 X. Wang, Y. Du and H. Liu, *Carbohydr. Polym.*, 2004, **56**, 21–26.
60 N. V. Kramareva, A. Y. Stakheev, O. P. Tkachenko, K. V. Klementiev, W. Grunert, E. D. Finashina and L. Kustov, *J. Mol. Catal. A: Chem.*, 2004, **209**, 97–106.
61 C. Díaz and M. L. Valenzuela, *Macromolecules*, 2006, **39**, 103–111.
62 M. Mohammadikish, *Ceram. Int.*, 2014, **40**, 1351–1358.
63 H. Liang, S. Jiang, Z. Qi, W. Chen, Z. Wu, B. Xu, Z. Wnah, J. Mi and Q. Li, *Nanoscale*, 2014, **6**, 7199–7203.
64 J. Bandara, U. Klehm and J. Kiwi, *Appl. Catal.*, 2007, **76**, 73–81.
65 M. Iwamoto, A. Takayuki and Y. Tachibana, *J. Mol. Catal. A: Chem.*, 2000, **155**, 143–153.
66 M. B. Fernandez van Raap, F. H. Sancehz, A. G. Leiva, M. L. Japas, E. Cabanillas and H. Troiani, *Physica B*, 2007, **398**, 229–234.
67 C. Rath, K. K. Sahu, S. D. Kulkarni, S. Anand, S. K. Date, R. P. Das and N. C. Mishra, *Appl. Phys. Lett.*, 1999, **75**, 4171–4173.
68 T. P. Raming, A. J. A. Winnnbust, C. M. Van Kats and A. P. Philipse, *J. Colloid Interface Sci.*, 2002, **249**, 346–350.
69 F. Wang, V. N. Richard, S. P. Shieds and W. E. Buhro, *Chem. Mater.*, 2014, **26**, 5–21.
70 C. Díaz, M. L. Valenzuela, V. Lavayen and C. O'Dwyer, *Inorg. Chem.*, 2012, **51**, 6228–6236.
71 E. Finney and R. Finke, *J. Colloid Interface Sci.*, 2008, **317**, 351–374.
72 C. Díaz, M. L. Valenzuela, L. Zuñiga and C. O'Dwyer, *J. Inorg. Organomet. Polym.*, 2009, **19**, 507–520.
73 Z. Cao, M. Qin, B. Jia, Y. Gu, P. Chen, A. Volinsky and X. Qu, *Ceram. Int.*, 2015, **41**, 2806–2812.
74 F. Harraz, A. Ismail, S. Al-Sayari and A. Al-Hajry, *J. Photochem. Photobiol., A*, 2015, **299**, 18–24.
75 A. Tian, Q. Xu, X. Shi, H. Yang, X. Xue, J. You, X. Wang, C. Dong, X. Yan and H. Zhou, *RSC Adv.*, 2015, **5**, 62724–62731.
76 P. Basnet, G. K. Larsen, R. P. Jadeja, Y. Hung and Y. Zhao, *ACS Appl. Mater. Interfaces*, 2013, **5**, 2085–2095.
77 G. K. Pradhan and K. M. Parida, *ACS Appl. Mater. Interfaces*, 2011, **3**, 317–323.
78 M. Miyauchi, A. Nakajima, T. Watanabe and K. Hashimoto, *Chem. Mater.*, 2002, **14**, 2812–2816.
79 A. Ayachi, H. Mechakra, M. Silvan, S. Boudjaadar and S. Achour, *Ceram. Int.*, 2015, **41**, 2228–2233.
80 S. J. Moniz, S. A. Shevlin, X. An, Z. X. Guo and J. Tang, *Chem. – Eur. J.*, 2014, **20**, 15571–15579.
81 L. Peng, T. Xie, Y. Lu, H. Fan and D. Wang, *Phys. Chem. Chem. Phys.*, 2010, 8033–8041.
82 M. Gupta Shipra and M. Tripathi, *Chin. Sci. Bull.*, 2011, 1639–1657.